Journal of Hazardous Materials 496 (2025) 139362

Contents lists available at ScienceDirect

Journal of Hazardous Materials

journal homepage: www.elsevier.com/locate/jhazmat

Decoupling adsorption affinity and regeneration barrier via dynamic electron redistribution in Fe-Zr metal-organic framework gels

Kaihuang Zhu [a,b,1], Chi Song [a,1], Guanqing Song [a,c], Jiajun Yu [a,c], Shijie Yang [a,c], Xiao Wang [a], Gansheng Shi [a], Zepeng Rao [d,e,*], Jianjun Liu [a], Jing Sun [a,**]

[a] State Key Lab of High Performance Ceramics and Superfine Microstructure, Shanghai Institute of Ceramics, Chinese Academy of Sciences, 585 Heshuo Road, Shanghai 201899, China
[b] College of Materials Science and Engineering, Shenyang University of Chemical Technology, Shenyang 110142, PR China
[c] University of Chinese Academy of Sciences, 19 (A) Yuquan Road, Beijing 100049, China
[d] Innovation Center of Yangtze River Delta, Zhejiang University, Zhejiang 311400, China
[e] Department of Environmental Science, Zhejiang University, Zhejiang 310058, China

HIGHLIGHTS

- FeU-1 achieves high toluene uptake and significantly reduced desorption energy.
- Dynamic asymmetric electron redistribution modulates metal···π interactions during adsorption-desorption.
- DFT and AIMD reveal desorption pathways and electron redistribution dynamics.
- The strategy is transferable to other dual-metal MOF gels, offering a general design concept.

GRAPHICAL ABSTRACT

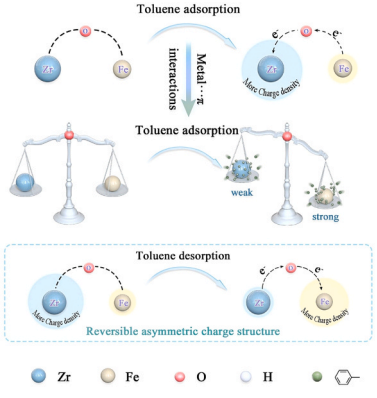

ARTICLE INFO

Keywords:
Dynamic electron redistribution
Low-energy regeneration
Metal-organic frameworks
Bimetallic metal-organic frameworks gels
Design universality
Volatile organic compounds
Sustainability

ABSTRACT

Amid global efforts toward low-energy gas purification, we present a bimetallic metal-organic framework gel (FeU-1) that overcomes the trade-off between adsorption capacity and regeneration energy. FeU-1 achieves a high toluene uptake of 975 mg/g ($P/P_0 = 0.97$), while reducing the desorption activation energy from 169.1 kJ/mol (UiO-66 MOF) to 34.9 kJ/mol. In situ DRIFTS and XPS analyses reveal dynamic electron migration between Fe and Zr nodes during the adsorption-desorption cycle, validating that the reversible asymmetric electron distribution modulates metal···π interactions. DFT and AIMD simulations further identify a "parallel" bimetallic adsorption configuration and track the complete desorption trajectory of toluene, highlighting the sequential detachment of molecules from different metal sites, governed by their interaction strengths. This electron-

* Corresponding author at: Innovation Center of Yangtze River Delta, Zhejiang University, Zhejiang 311400, China.
** Corresponding author.
E-mail addresses: raozepeng@zju.edu.cn (Z. Rao), jingsun@mail.sic.ac.cn (J. Sun).
[1] These authors contributed equally to this work.

https://doi.org/10.1016/j.jhazmat.2025.139362
Received 6 May 2025; Received in revised form 26 June 2025; Accepted 25 July 2025
Available online 31 July 2025

regulation mechanism, validated in CuU-1 and AlU-1, offers a broadly applicable strategy for designing other open-shell bimetallic MOGs with tunable adsorption-desorption behavior. This work deepens the understanding of charge-regulated host–guest interactions and proposes a rational strategy for designing intelligent, energy-efficient VOC adsorbents aligned with global carbon neutrality goals.

1. Introduction

Toluene, a representative aromatic volatile organic compound (VOC), is primarily emitted from industrial activities such as petroleum refining and fossil fuel combustion, posing significant risks to human health and the environment[12,17,27]. Among the various treatment strategies, Adsorption is widely recognized as one of the most convenient and cost-effective methods for toluene removal, with broad industrial applicability[36]. However, while several adsorbents with high adsorption capacities for toluene have been developed, their strong adsorption affinities often lead to increased regeneration energy demands, limiting practical efficiency and sustainability[26].

The adsorption and desorption of toluene are governed by complex host-guest interactions, including metal···π, C-H···π, and π···π interactions, along with spatial structural effects[6]. Recent studies have highlighted the potential of open metal centers as effective adsorption sites for aromatic VOCs, offering promising avenues for improving adsorption efficiency and desorption performance[15,2,7,9]. Building upon these insights, this work aims to design a porous framework that balances strong adsorption capacity with facile regeneration, thereby addressing a key challenge in VOC abatement.

The electron-rich nature of the aromatic ring in toluene allows it to preferentially adsorb onto open metal sites[38], where metal···π interaction, primarily driven by electrostatic forces, enhances adsorption strength through electron sharing between metal nodes and toluene molecules[24]. This mechanism has been extensively investigated and applied in various adsorbents over recent years[14,21,29]. However, most previous studies have not addressed the simultaneous optimization of adsorption strength and regeneration efficiency often conflicting requirements in practical applications.

Metal-organic framework gels (MOGs), derived from Metal-organic frameworks (MOFs), retain key structural and functional advantages such as high surface area, tunable pore size, low density, and modifiable internal surfaces, making them promising candidates for adsorption and separation applications[1,11,19,20,33,4]. Beyond these benefits, MOGs exhibit unique hierarchical pore architectures and enhanced structural flexibility. In particular, the integration of bimetallic nodes into MOGs introduces new possibilities for regulating metal···π interactions. Specifically, electron transfer between open-shell bimetallic nodes stabilizes structural states during the adsorption-desorption cycle, generating localized asymmetric electron distribution[5,6,18,23,30]. These asymmetry structures provide a promising strategy for the precise modulation of metal···π interactions, effectively optimizing adsorption strength and desorption behavior.

We report a novel bimetallic metal-organic gel (MOG), designated as FeU-1, synthesized by incorporating Fe into UiO-66 MOG framework via a one-step process, partially substituting Zr in the original Zr_6-oxo cluster. Unlike conventional MOFs, FeU-1 features bimetallic nodes with reduced coordination to organic linkers, thereby intensifying host-guest interactions with toluene, primarily driven by metal···π interactions [37]. The open-shell Fe and Zr metal nodes serve as primary adsorption sites, functioning as electron donor-acceptor pairs to form localized asymmetric electron distributions[23]. This asymmetric structure facilitates dynamic electron transfer between metal centers, optimizing interactions with toluene while maintaining structural stability throughout adsorption-desorption cycles. FeU-1 achieves a saturated adsorption capacity of 975.4 mg/g at a relative pressure of $P/P_0 = 0.9$, coupled with a significantly reduced desorption activation energy of 34.9 kJ/mol, thus lowering regeneration energy requirements. Additionally, a series of bimetallic MOGs (such as Zr-Cu, and Zr-Al) were successfully synthesized, showcasing tunable electronic properties and adjustable metal···π interactions during toluene adsorption-desorption cycles. This study introduces a novel strategy for engineering bimetallic nodes to enhance adsorption performance and reduce regeneration energy consumption, paving the way for development of high-performance toluene adsorbent materials.

2. Results and discussion

2.1. Toluene adsorption-desorption performance

Static toluene adsorption experiments at 298 K (Fig. 1a) revealed that the activated FeU-1 achieved an exceptional saturated adsorption capacity of 975.4 mg/g, significantly surpassing UiO-66 MOF (471.5 mg/g) and UiO-66 MOG (882.6 mg/g). Compared with previously reported materials (Fig. 1e, Table S4), FeU-1 shows markedly superior toluene adsorption capacity, underscoring its potential for applications such as petroleum refining processes or managing organic solvent tank leakages. Dynamic breakthrough experiments with 100 ppm toluene further validated the adsorption performance of FeU-1 (Fig. 1b). FeU-1 exhibited the highest adsorption capacity (112.6 mg/g), consistent with static adsorption results. Notably, during the initial adsorption phase, FeU-1 (Figure S1) maintained 100 % toluene removal efficiency demonstrating rapid adsorption kinetics and strong response capability for toluene. While high adsorption capacity is generally linked to high regeneration energy requirements[16], the temperature-programmed desorption (TPD) measurements (Figure S2) at varying heating rates revealed that FeU-1 (Fig. 1c) possesses the lowest desorption activation energy (E_d = 34.9 kJ/mol), significantly lower than UiO-66 MOF and UiO-66 MOG. This indicates that FeU-1 facilitates easier toluene desorption. Moreover, FeU-1 retained a high adsorption capacity of 871.3 mg/g after four regeneration cycles (Fig. 1d), demonstrating exceptional stability. These findings highlight FeU-1's ability to achieve high adsorption performance while minimizing regeneration energy requirements, positioning it as a promising candidate for efficient toluene capture and recovery.

2.2. Significance of low-coordination structure

The enhanced adsorption performance of FeU-1 is attributed to defect engineering (low-coordination structural) introduced during in-situ synthesis. A competitive coordination strategy enabled the partial substitution of Zr ions in the Zr_6-oxo cluster with Fe. Powder X-ray diffraction (PXRD) patterns (Figure S3) displayed a shift in FeU-1's characteristic peaks to higher angles[10], confirming successful synthesis. X-ray photoelectron spectroscopy (XPS) revealed charge transfer at the Fe and Zr bimetallic nodes. Specifically, the Fe 2p spectrum showed the presence of the Fe^{2+} peak (Fig. 2a), indicating the reduction of Fe^{3+} to Fe^{2+}. Concurrently, the Zr $3d_{5/2}$ and Zr $3d_{3/2}$ peaks (Fig. 2c) shift to higher binding energies, while the O_{lat} peak (Fig. 2b) shifts by 0.29 eV to lower binding energy, illustrating an electron transfer pathway from Zr to Fe via the oxy-bridged linkages. X-ray absorption spectroscopy (XAS) analysis further supports this conclusion. The Fe K-edge XANES spectrum of FeU-1 (Fig. 2d) closely resembles that of Fe_3O_4, confirming the presence of Fe in mixed Fe^{2+}/Fe^{3+} oxidation states[31,34]. Extended X-ray absorption fine structure (EXAFS, Fig. 2e) and wavelet transform (WT) analyses (Fig. 2g) revealed a new peak at 3.10 Å in R-space, attributed to Fe-Zr scattering. K-space and R-space

fitting (Fig. 2c, Figure S4, Table S1) indicated a reduced oxygen coordination around Fe, confirming defect formation. The Fe-Zr coordination number of 4 validates the successful incorporation of Fe into the Zr_6-oxo cluster, replacing two Zr ions to form Zr-O-Fe linkages. These structural modifications are consistent with the Fe: Zr ratio of 1:1.94 determined by ICP analysis (Table S2) and corroborated by thermogravimetric analysis (TGA) and Brunauer-Emmett-Teller (BET) measurements (Figure S5-6, Table S3). Scanning electron microscopy (SEM) images (Fig. 2h, Figure S7) further confirm the low-coordination structural characteristics of FeU-1, highlighting the critical role of this feature in its enhanced adsorption performance.

2.3. Mechanism of toluene adsorption-desorption

The low-coordination structure of FeU-1 reduces π···π interactions between the organic ligands and toluene while simultaneously enhancing metal···π interactions through the exposure of highly accessible metal sites[35]. NH_3-TPD results (Figure S8) confirmed an increase

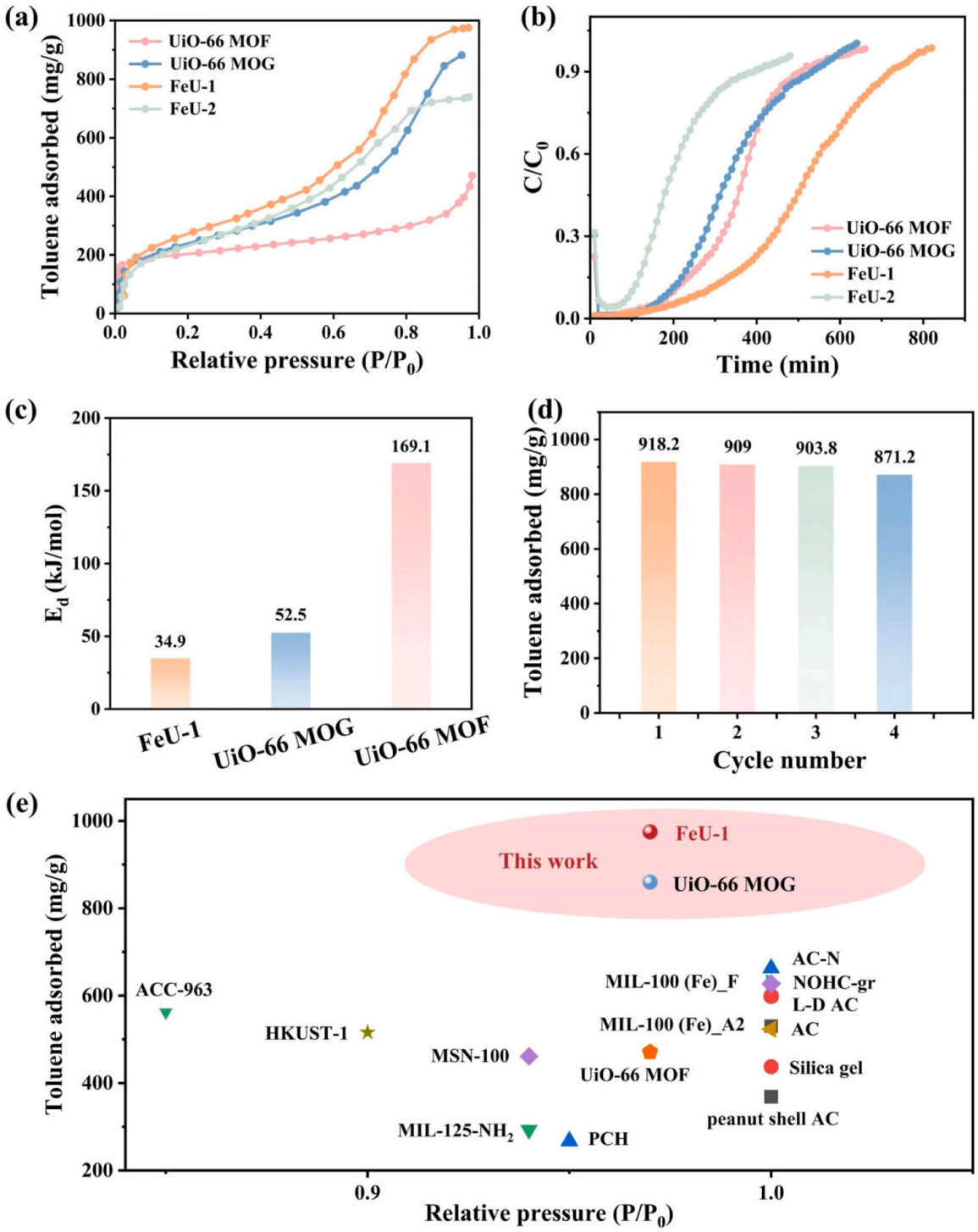

Fig. 1. (a) Adsorption isotherms of toluene vapor on UiO-66 MOF, UiO-66 MOG, FeU-1, FeU-2. (b) Toluene adsorption breakthrough curves of UiO-66 MOF, UiO-66 MOG, FeU-1, FeU-2. (c) Desorption activation energy of UiO-66 MOF, UiO-66 MOG, FeU-1. (d) Cycling performance test of FeU-1 over multiple adsorption-desorption cycles. (e) Adsorbed toluene amounts on FeU-1 and UiO-66 MOG compared with porous sorbents reported in the literature at high-pressure range.

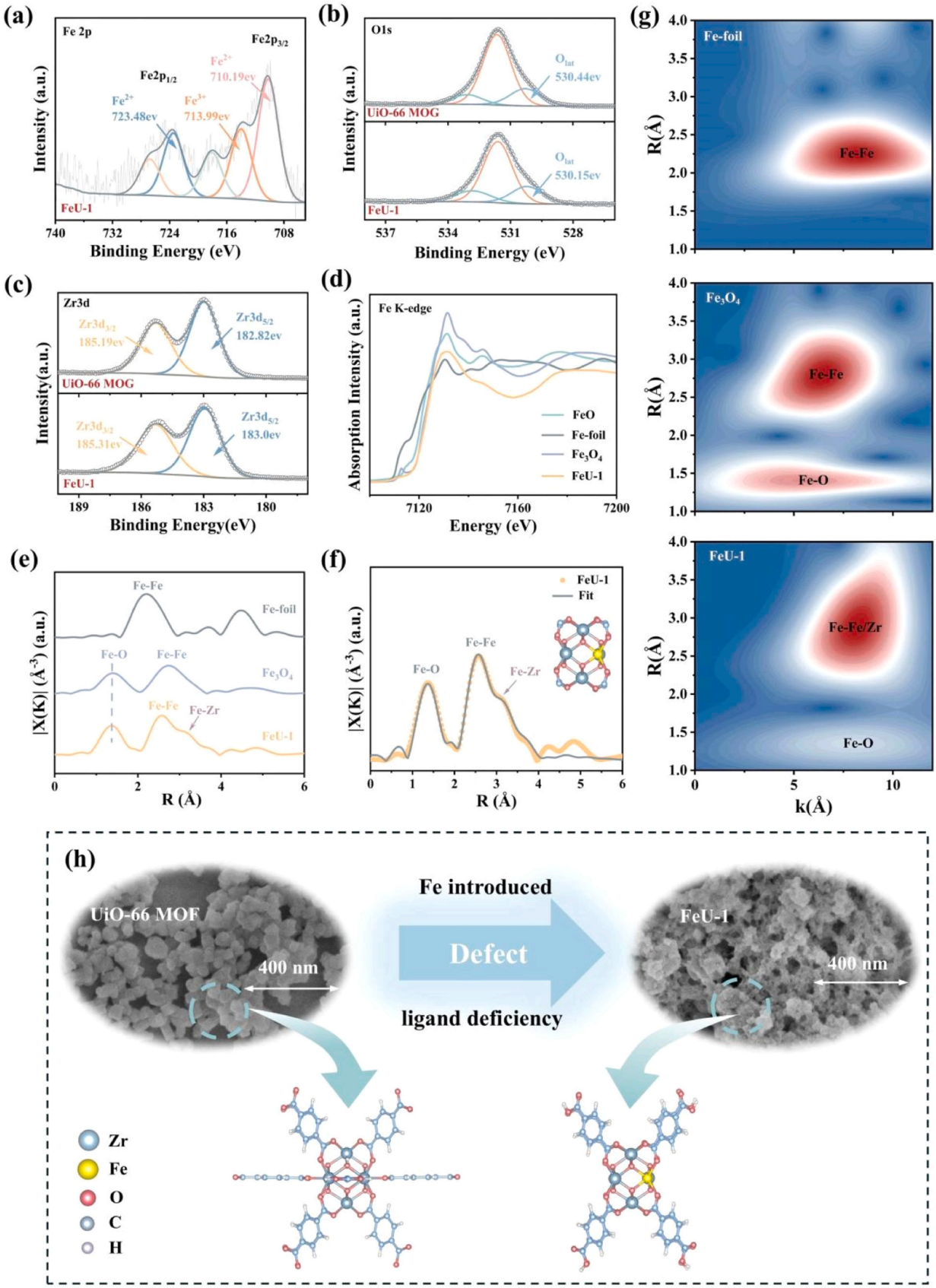

Fig. 2. High-resolution XPS spectra of (a) Fe 2p, (b) O 1 s, and (c) Zr 3d in UiO-66 MOG, FeU-1. (d) Fe K-edge XANES spectra and (e) transformed EXAFS spectra of FeU-1, Fe_3O_4, and Fe-foil. (f) EXAFS and its fitting curve of FeU-1 (inset red: O, blue: Zr, yellow: Fe). (g) WT-EXAFS of Fe-foil, Fe_3O_4, FeU-1. (h) SEM images of UiO-66 MOF and FeU-1, along with the enlarged view of secondary building units (SBUs), reveal that the incorporation of Fe induces ligand dissociation in FeU-1, leading to low-coordination structures.

in unsaturated metal sites in FeU-1. This finding aligns with adsorption isotherms measured at different temperatures (Figure S9a-b) and the calculated adsorption enthalpy (Q_{st}) (Figure S9e), which collectively demonstrate that the introduction of Fe significantly strengthens host-guest interactions between the adsorbent and toluene. In-situ DRIFT spectra (Fig. 3a) further elucidated the role of metal nodes during toluene adsorption. Over time, the intensities of the Fe-O (550 cm^{-1}) [13] bond and Zr-O (644 cm^{-1})[25] bond vibrations exhibited significant variations, while the aromatic C═C skeletal vibration (1450–1650 cm^{-1})[3] remained largely unchanged, indicating that

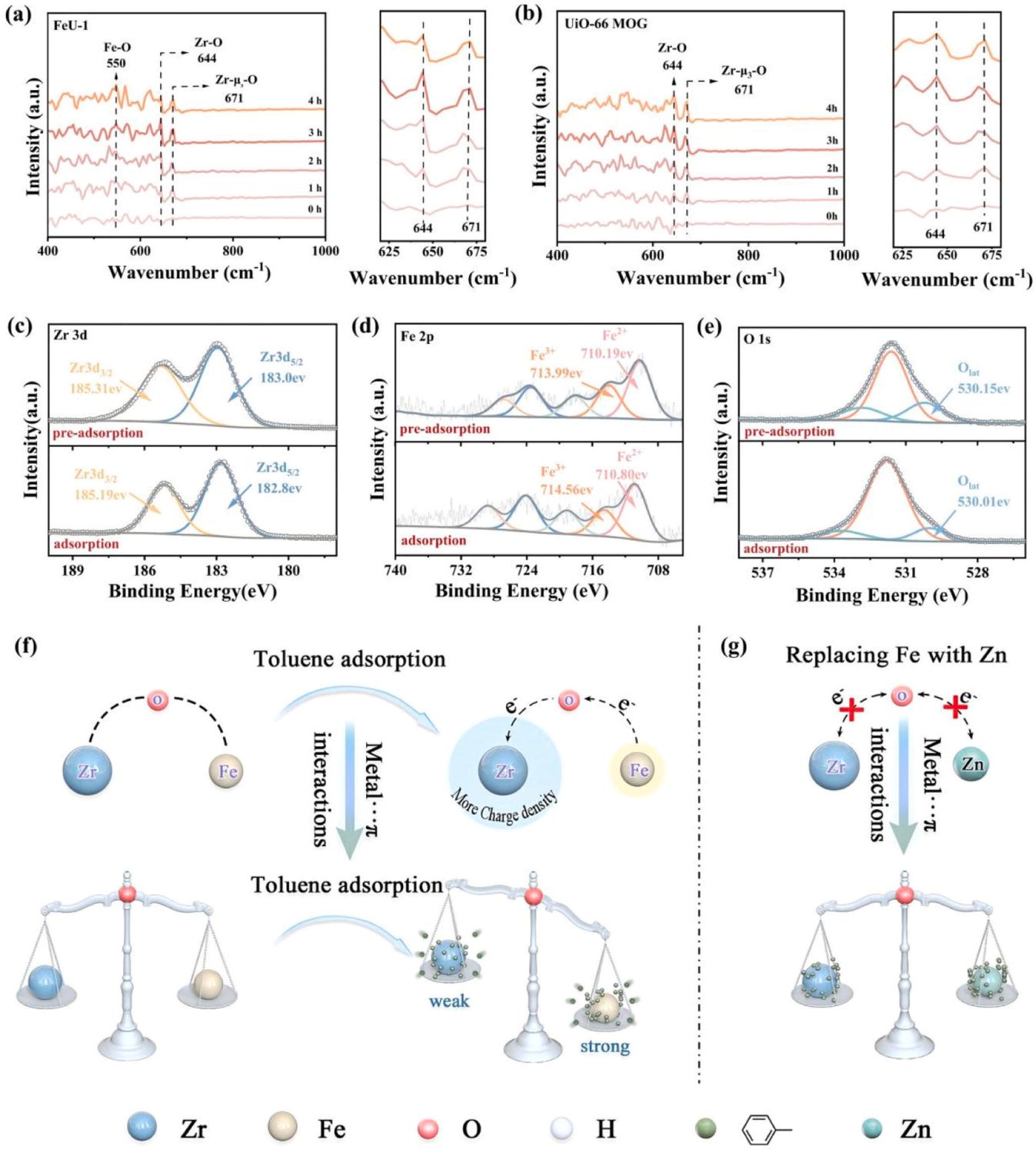

Fig. 3. In-situ DRIFT spectra showing adsorbed toluene over time for (a) FeU-1 and (b) UiO-66 MOG, with the inset highlighting the magnified view of Zr-O (644 cm^{-1}) and Zr-μ_3-O (671 cm^{-1}) bond vibrations. Electron transfer process in the open-shell bimetallic nodes of FeU-1 after toluene adsorption. XPS spectra of (c) Zr 3d, (d) Fe 2p, and (e) O 1 s in FeU-1 before and after toluene adsorption. (f) Schematic illustration depicting electron transfer pathways and dynamic changes in metal···π interactions between metal adsorption sites and toluene in FeU-1. (g) Comparative schematic representation of ZnU-1 with closed-shell Zn nodes versus FeU-1 after toluene adsorption, illustrating structural and electronic differences.

metal···π interactions predominantly govern the adsorption process. Notably, after 3 h of adsorption, the Zr-O peak intensity decreased, suggesting a reduced role of Zr sites in binding toluene. This behavior is absent in the control sample (UiO-66 MOG), as shown in Fig. 3b, indicating that the asymmetric structure of FeU-1's metal nodes lead to distinct adsorption behaviors. These findings highlight the critical role of the low-coordination structure in modulating the adsorption-desorption mechanism, wherein the exposed metal sites and dynamic electron distributions in FeU-1 enhance metal···π interactions while adapting adsorption forces to optimize performance.

XPS analysis of FeU-1 before and after toluene adsorption (Fig. 3c-e) revealed notable charge distribution differences between Fe and Zr nodes. Fe exhibited stronger electron-donating ability, while Zr preferentially acts as an electron acceptor. Upon toluene adsorption, the Zr 3d peaks (Fig. 3c) shifted to lower binding energies, indicating electron density gain at Zr sites. In contrast, the spin-split peaks in the Fe 2p spectrum (Fig. 3d) shifted to higher binding energies, reflecting electron density loss at Fe sites. These shifts confirmed the spontaneous formation of a local asymmetric electron distribution within the metal nodes of FeU-1 (Fig. 3f). As electron transfer progresses during adsorption (Fig. 3f), the interaction between Fe nodes and toluene becomes stronger, while the interaction at Zr nodes gradually diminishes. This dynamic modulation of electron transfer highlights the critical role of FeU-1's asymmetric structure in optimizing adsorption performance.

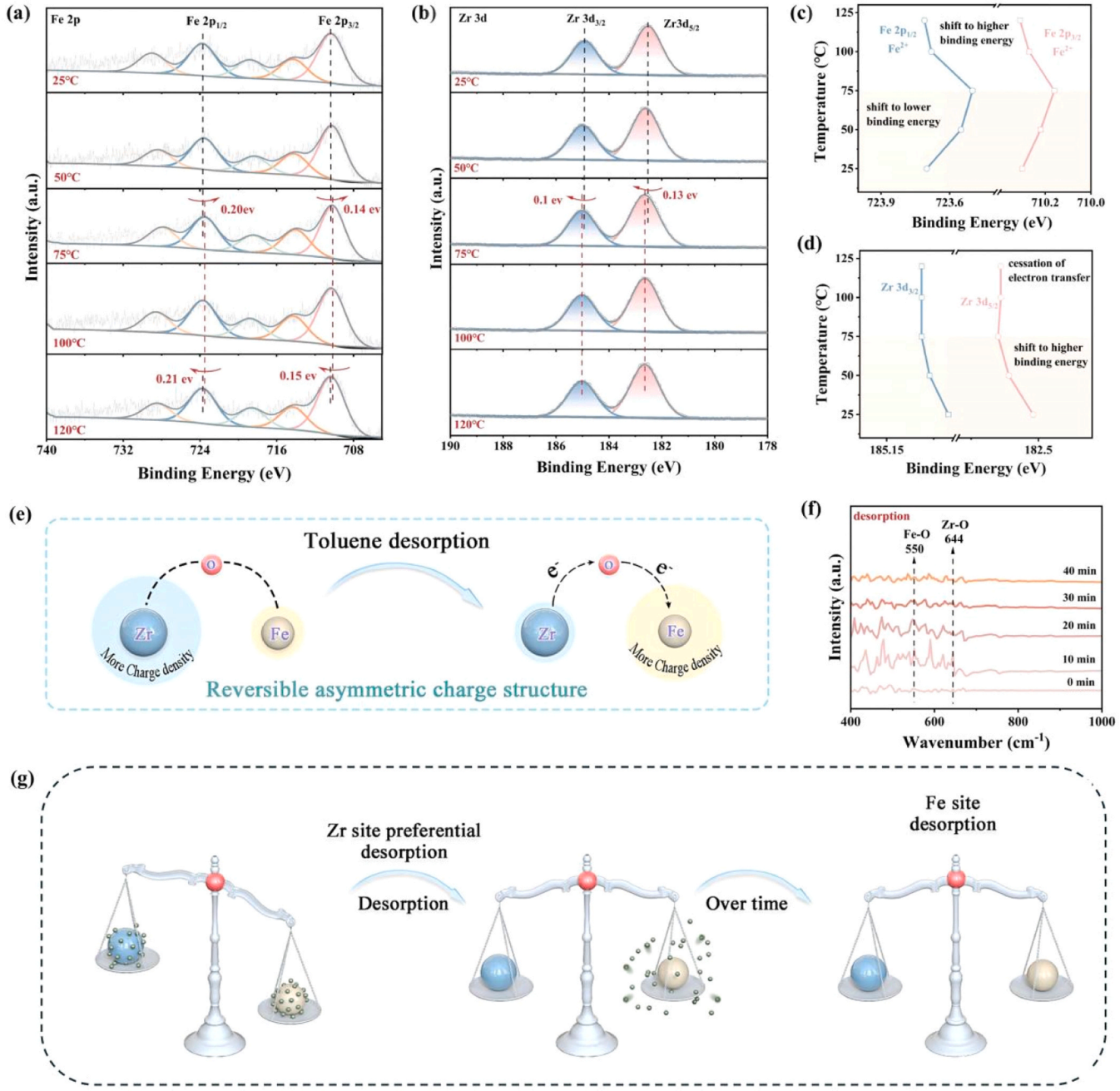

Fig. 4. (a) In-situ XPS of Fe 2p during toluene desorption from FeU-1 at temperatures ranging from 25 °C to 120 °C. (b) In-situ XPS spectra of Zr 3d during toluene desorption from FeU-1 across the same temperature range. Trends of binding energy of (c) Fe 2p and (d) Zr 3d peaks with temperature in In-situ XPS. (e) Schematic representation of electron transfer dynamics during toluene desorption from FeU-1, illustrating the reversibility of the asymmetric electron distribution at FeU-1 metal nodes. (f) In-situ DRIFT spectra of toluene desorption from FeU-1 at 100℃. (g) Sequential desorption of toluene from Zr and Fe sites, driven by variations in the strength of electrostatic interactions between FeU-1 and toluene.

To validate the pivotal of open-shell metal nodes in modulating adsorption forces, a control experiment was conducted by substituting Fe in FeU-1 with Zn under identical synthesis conditions (Figure S10). Unlike open-shell Fe sites, Zn is a closed-shell metal incapable of accommodating additional electrons. XPS analysis (Figure S11) confirmed this, as the binding energy of the metal nodes in ZnU-1 remained unchanged before and after toluene adsorption, indicating the absence of electron transfer involving Zn nodes[23]. Further evidence from the in-situ DRIFT spectra during toluene adsorption (Figure S12) revealed marked differences between ZnU-1 and FeU-1. The intensity of Zn-O (540 cm^{-1})[22,8] and Zr-O (644 cm^{-1}) peaks in ZnU-1 increased steadily over time, suggesting a static adsorption mechanism. In contrast, FeU-1 (Fig. 3c-d) exhibited dynamic modulation of adsorption forces, driven by electron transfer between Fe and Zr nodes. These findings (Fig. 3g) underscore the unique contribution of open-shell metal nodes in enhancing adsorption performance through dynamic adjustment of host-guest interactions.

As previously described, the dynamic electron modulation between

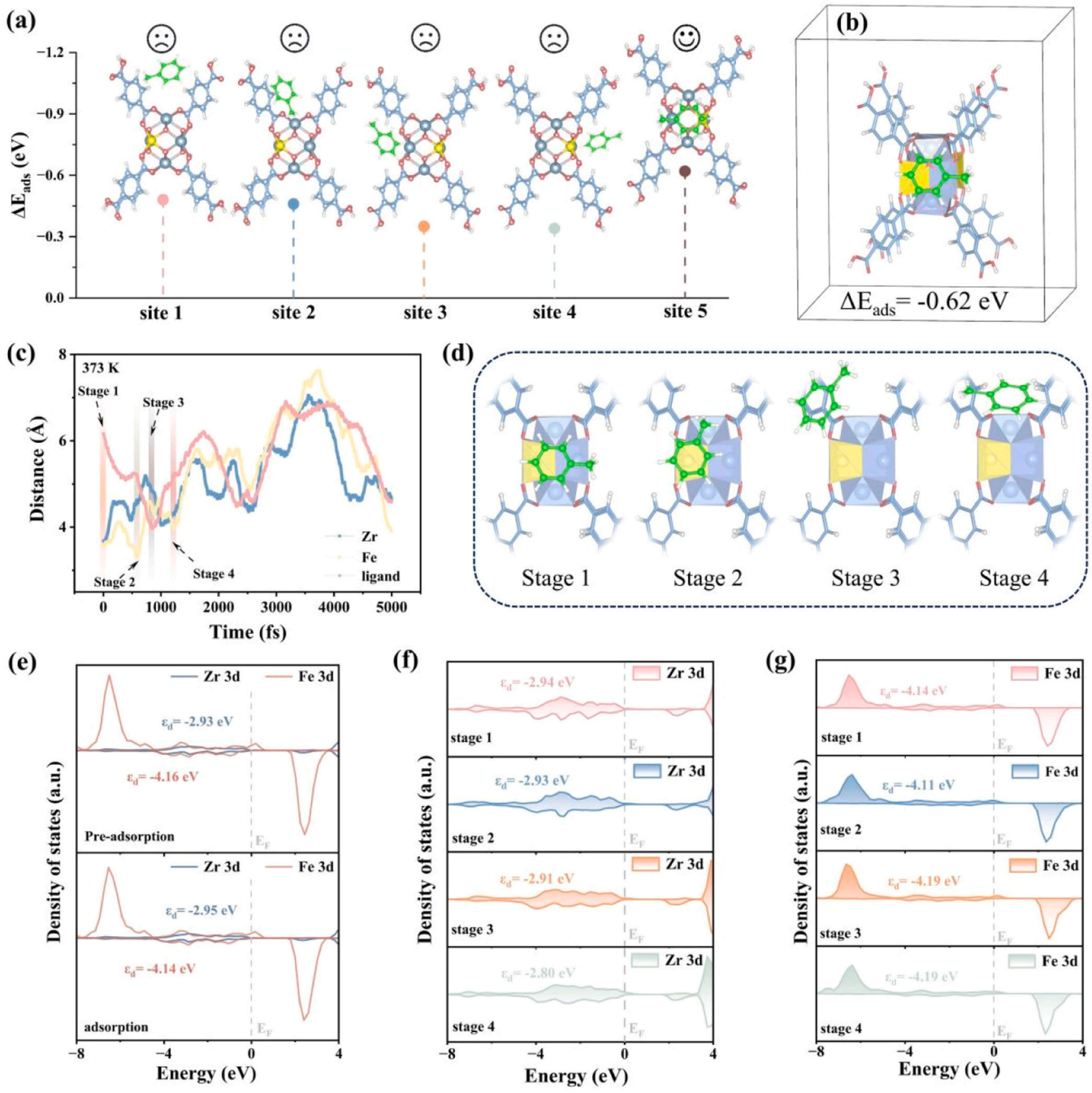

Fig. 5. Adsorption configuration and performance of toluene in FeU-1. (a) DFT-calculated adsorption energies of toluene in various configurations: terminal Zr node (site 1), benzene ring of the organic ligand (site 2), Zr node (site 3), Fe node (site 4), and (site 5) bimetallic cooperative adsorption (red: O, blue: Zr, yellow: Fe). (b) Toluene molecules preferentially adopt a parallel adsorption configuration on bimetallic (yellow polyhedral: Fe, blue polyhedral: Zr) sites. (c) Distance of toluene molecules from metal sites and ligands in FeU-1 over MD simulation time at 373 K, illustrating the thermal desorption of toluene from FeU-1, the corresponding system is shown in panel (d), representing (green: toluene) four stages: 1 (initiation of desorption), 2 (detachment from Zr nodes), 3 (π···π interactions), and 4 (complete desorption). (e) Calculated PDOS of Fe and Zr d-bands in FeU-1 before and after toluene adsorption. PDOS of (f) Zr d-band and (g) Fe d-band at four stages of toluene desorption on FeU-1 at 373 K.

bimetallic nodes in FeU-1 is pivotal in regulating the electrostatic interactions between toluene molecules and adsorption sites. Notably, after toluene adsorption, the electron enrichment at Zr sites weakens the metal···π interaction with toluene, thereby enabling easier desorption from these sites compared to those with stronger binding. In-situ DRIFT spectra (Fig. 4f) during toluene desorption at 100°C revealed that the intensity changes of the Zr-O bond (644 cm^{-1}) were more pronounced and stabilized earlier than those of the Fe-O bond (550 cm^{-1}), indicating preferential desorption of toluene from Zr sites. Furthermore, in-situ temperature-programmed XPS analysis (Fig. 4a-b) of FeU-1 after toluene adsorption demonstrated the reversibility of the asymmetric electron distribution between the bimetallic nodes. As the temperature increased from 0°C to 75°C, the Fe^{2+} peak (Fig. 4c) in the Fe 2p spectrum shifted to lower binding energy, while the Zr 3d peak (Fig. 4d) shifted to higher binding energy, signifying (Fig. 4e) electron migration from Zr to Fe via oxy-bridge[32]. This electron transfer weakens the metal···π interaction between Fe sites and toluene, resulting promotes toluene desorption from Fe sites. Upon further heating (75°C-120℃), the Zr 3d peak (Fig. 4d) remained unchanged, suggesting stabilization of the electronic state around Zr sites and cessation of electron transfer. In contrast, as toluene progressively desorbed from Fe sites, the electron density surrounding Fe nodes decreased, causing the Fe^{2+} peak (Fig. 4c) to shift to higher binding energy. These observations (Fig. 4g) provide compelling evidence for a sequential desorption process, wherein toluene molecules detach from FeU-1 adsorption sites in a hierarchical manner dictated by the strength of metal···π interactions. This sequential desorption reflects the critical role of asymmetric electron distribution in modulating adsorption and desorption dynamics in FeU-1.

Based on structural characterization, the adsorption energy of toluene at various sites in FeU-1 was calculated using density functional theory (DFT) (Fig. 5a). The results indicated (Fig. 5b) that FeU-1 preferentially adsorbed toluene molecules via metal···π interactions, with the molecules adopting a "parallel" adsorption configuration on the bimetallic nodes. This behavior is attributed to the absence of organic ligands in FeU-1, which exposes additional open metal sites, increasing adsorption space and significantly enhancing adsorption capacity. Ab initio molecular dynamics (AIMD) simulations at different temperatures revealed (Fig. 5c, Figure S13-15, Video S1–3) that toluene molecules can readily desorb from the bimetallic adsorption sites at 373 K. The desorption process, analyzed through Supplementary Video S3, indicated a sequential transition: during stages 1–2 (Fig. 5d), toluene shifted from dual-node adsorption to exclusive binding at Fe sites; in stage 3, the adsorption evolved into π···π interactions involving the aromatic ring, culminating in complete desorption in stage 4. These AIMD findings corroborate in-situ XPS observations of preferential desorption from Zr sites at elevated temperatures, providing a mechanistic explanation for the dynamic behavior. Collectively, these results elucidate the critical role of bimetallic nodes in regulating adsorption and desorption processes, and validate the dynamic tunability of FeU-1, highlighting its potential for enhanced toluene adsorption-desorption performance.

In addition, density of states (DOS) analysis (Figure S16-20) reveals that electron migration between bimetallic sites in FeU-1 during toluene adsorption and desorption is primarily associated with the d-electrons of metal atoms. As shown in Fig. 5e, the projected density of states (PDOS) of the Zr and Fe d-orbitals shifts upon toluene adsorption, with the Zr d-band center moving from −2.93 eV to −2.95 eV and the Fe d-band center shifting from −4.16 eV to −4.14 eV, confirming electron transfer from Fe to Zr[28,39]. To explore the electronic structure at the bimetallic adsorption sites of FeU-1 during the four stages of toluene desorption, the projected density of states (PDOS) for the Fe atomic orbitals were computed at each stage. The results reveal distinct electronic behaviors at the bimetallic nodes of FeU-1. The right shift of the Zr d-band center (Fig. 5f) indicates an increased electron-donating ability of Zr sites. Notably, the Fe d-band center also shifts rightward from stage 1 to stage 2 (Fig. 5g), suggesting a transition from bimetallic cooperative adsorption (stage 1) to a single-site adsorption mode at the Fe site. (stage 2). In the subsequent stages 2 and 3, the leftward shift of the Fe d-band center (Fig. 5g) indicates that the Fe site becomes more electron-accepting. The toluene adsorption and desorption process in FeU-1 further demonstrates a reversible transition of the Fe and Zr nodes between electron donor and acceptor roles, significantly affecting the adsorption and desorption behavior of toluene.

2.4. Strategy generalizability

To validate the generality of electron transfer between open-shell metals in modulating adsorption interaction with toluene molecules, three additional bimetallic MOGs, such as ZnU-1, AlU-1, and CuU-1, were synthesized. XRD patterns showed characteristic peak shifts (Figure S21, Figure S24), confirming the successful incorporation of these open-shell metals into the Zr_6-oxo framework. XPS analysis (Figure S22, Figure S26) revealed that toluene adsorption reduced electron transfer between the bimetallic nodes, evidenced by binding energy shifts before and after adsorption. Additionally, in-situ DRIFT spectra (Figure S23, Figure S25) during adsorption demonstrated a gradual decrease in the intensity of the Zr-O peak for all three MOGs with increasing adsorption time, signifying a reduced contribution of Zr nodes to toluene adsorption. This behavior is consistent with observations from FeU-1, highlighting the universal applicability of this electron transfer mechanism in bimetallic MOGs.

3. Conclusion

This work demonstrates that low-coordination open-shell metal nodes exhibit exceptional adsorption capacity for toluene, primarily driven by metal···π interactions. During the adsorption-desorption process, electron transfer between metal nodes dynamically modulates these interactions, enhancing the affinity for toluene while simultaneously reducing the desorption activation energy. Based on these findings, we propose the construction of bimetallic nodes with a localized asymmetric electron distribution structure, leveraging the reversible nature of these centers to induce differential adsorption strengths among metal nodes. This strategy holds significant potential for designing advanced adsorbents with high adsorption capacities and energy-efficient desorption properties.

CRediT authorship contribution statement

Gansheng Shi: Validation. **Zepeng Rao:** Supervision. **Kaihuang Zhu:** Writing – review & editing, Writing – original draft, Project administration, Methodology, Investigation. **Jianjun Liu:** Software. **Jing Sun:** Validation, Supervision, Investigation, Funding acquisition, Formal analysis, Data curation. **Jiajun Yu:** Supervision. **Shijie Yang:** Supervision. **Chi Song:** Validation, Software. **Guanqing Song:** Visualization, Validation, Methodology. **Xiao Wang:** Supervision.

Declaration of Competing Interest

The authors declare that they have no known competing financial interests or personal relationships that could have appeared to influence the work reported in this paper.

Appendix A. Supporting information

Supplementary data associated with this article can be found in the online version at doi:10.1016/j.jhazmat.2025.139362.

Data availability

Data will be made available on request.

References

[1] Bi, F., Wei, J., Gao, B., Ma, S., Liu, N., Xu, J., Liu, B., Huang, Y., Zhang, X., 2024. How the most neglected residual species in MOF-Based catalysts involved in catalytic reactions to form toxic byproducts. Environ Sci Technol 58 (44), 19797–19806. https://doi.org/10.1021/acs.est.4c06351.

[2] Cao, J., Li, Y., Ma, X., Qi, M., Liu, B., Zhao, D., Wang, Y., 2025. Constructing binuclear sites to modulate the charge distribution of MIL-101 for enhanced toluene adsorption performance: experimental and theoretical studies. Sep Purif Technol 354, 129400. https://doi.org/10.1016/j.seppur.2024.129400.

[3] Chen, L., Wang, X., Rao, Z., Tang, Z., Shi, G., Wang, Y., Lu, G., Xie, X., Chen, D., Sun, J., 2022. One-pot synthesis of the MIL-100 (Fe) MOF/MOX homojunctions with tunable hierarchical pores for the photocatalytic removal of BTXS. Appl Catal B Environ 303, 120885. https://doi.org/10.1016/j.apcatb.2021.120885.

[4] Chen, L., Wang, X., Shi, G., Lu, G., Wang, Y., Xie, X., Chen, D., Sun, J., 2023. The regulation of lewis acid/basic sites in NaFe bimetal MOXs for the controllable photocatalytic degradation of electron-rich/deficient VOCs. Appl Catal B Environ 334, 122850. https://doi.org/10.1016/j.apcatb.2023.122850.

[5] Chen, Z., Fang, P., Li, J., Han, X., Huang, W., Cui, W., Liu, Z., Warren, M.R., Allan, D., Cheng, P., Yang, S., Shi, W., 2024. Rapid extraction of trace benzene by a crown-ether-based metal-organic framework. Natl Sci Rev 11 (12). https://doi.org/10.1093/nsr/nwae342.

[6] Di, J., Chen, C., Wu, Y., Chen, H., Xiong, J., Long, R., Li, S., Song, L., Jiang, W., Liu, Z., 2024. Asymmetric electron redistribution in Niobic-Oxygen vacancy associates to tune noncovalent interaction in CO_2 photoreduction. Adv Mater 36 (25), 2401914. https://doi.org/10.1002/adma.202401914.

[7] Fang, Z., Dürholt, J.P., Kauer, M., Zhang, W., Lochenie, C., Jee, B., Albada, B., Metzler-Nolte, N., Pöppl, A., Weber, B., Muhler, M., Wang, Y., Schmid, R., Fischer, R.A., 2014. Structural complexity in Metal–Organic frameworks: simultaneous modification of open metal sites and hierarchical porosity by systematic doping with defective linkers. J Am Chem Soc 136 (27), 9627–9636. https://doi.org/10.1021/ja503218j.

[8] Gupta, N.K., Bae, J., Kim, S., Kim, K.S., 2021. Fabrication of Zn-MOF/ZnO nanocomposites for room temperature H_2S removal: adsorption, regeneration, and mechanism. Chemosphere 274, 129789. https://doi.org/10.1016/j.chemosphere.2021.129789.

[9] Han, Y., Huang, W., He, M., An, B., Chen, Y., Han, X., An, L., Kippax-Jones, M., Li, J., Yang, Y., Frogley, M.D., Li, C., Crawshaw, D., Manuel, P., Rudić, S., Cheng, Y., Silverwood, I., Daemen, L.L., Ramirez-Cuesta, A.J., Day, S.J., Thompson, S.P., Spencer, B.F., Nikiel, M., Lee, D., Schröder, M., Yang, S., 2024. Trace benzene capture by decoration of structural defects in metal–organic framework materials. Nat Mater 23 (11), 1531–1538. https://doi.org/10.1038/s41563-024-02029-1.

[10] He, L., Yang, Z., Lu, X., Xu, Y., Yao, X., Li, C., Wu, C., Yao, Z., 2023. Defective UiO-66 by metal doping for highly efficient photocatalytic degradation of methyl mercaptan. J Environ Chem Eng 11 (6), 111419. https://doi.org/10.1016/j.jece.2023.111419.

[11] Hou, J., Sapnik, A.F., Bennett, T.D., 2020. Metal–organic framework gels and monoliths. Chem Sci 11 (2), 310–323. https://doi.org/10.1039/c9sc04961d.

[12] Huang, J., Feng, X., Bi, F., Huang, G., Rao, R., Qiao, R., Zhang, X., 2025. Strategic defect engineering in TiO_2 catalysts through electron beam irradiation: unraveling enhanced photocatalytic pathways for multicomponent VOCs degradation. Sep Purif Technol 359, 130804. https://doi.org/10.1016/j.seppur.2024.130804.

[13] Ji, W., Li, W., Wang, Y., Zhang, T.C., Wei, Y., Yuan, S., 2024. Zr-doped MIL-101 (Fe)/Graphene oxide nanocomposites: an efficient and water-stable MOF-based adsorbent for As(V) adsorption in aqueous solution. Sep Purif Technol 339, 126681. https://doi.org/10.1016/j.seppur.2024.126681.

[14] Jiang, B., Wang, W., Zhang, Y., Lu, Y., Zhang, C.W., Yin, G.Q., Zhao, X.L., Xu, L., Tan, H., Li, X., Jin, G.X., Yang, H.B., 2017. Construction of π-Surface-Metalated Pillar[5]arenes which bind anions via Anion–π interactions. Angew Chem Int Ed 56 (46), 14438–14442. https://doi.org/10.1002/anie.201707209.

[15] Kökçam-Demir, Ü., Goldman, A., Esrafili, L., Gharib, M., Morsali, A., Weingart, O., Janiak, C., 2020. Coordinatively unsaturated metal sites (open metal sites) in metal–organic frameworks: design and applications. Chem Soc Rev 49 (9), 2751–2798. https://doi.org/10.1039/C9CS00609E.

[16] Li, S., Subhan, S., Zhou, L., Li, J., Zhao, Z., Zhao, Z., 2023. High efficiency of toluene Ad-/Desorption on Thermal-conductive HKUST-1@BN nanosheets composite. Chem Eng J 465, 142791. https://doi.org/10.1016/j.cej.2023.142791.

[17] Liu, B., Zhao, W., Jiang, Q., Ao, Z., An, T., 2019. Enhanced adsorption mechanism of carbonyl-containing volatile organic compounds on Al-decorated porous graphene monolayer: a density functional theory calculation study. Sustain Mater Technol 21, e00103. https://doi.org/10.1016/j.susmat.2019.e00103.

[18] Liu, H., Yang, S., Mi, J., Sun, C., Chen, J., Li, J., 2024. 4d–2p–4f gradient orbital coupling enables tandem catalysis for simultaneous abatement of N_2O and CO on atomically dispersed rh/CeO_2 catalyst. Environmental Science Technology 58(38) 1712517136. https://doi.org/10.1021/acs.est.4c02277.

[19] Liu, N., Tian, M., Zhang, Y., Yang, J., Wang, Z., Dai, W., Quan, G., Lei, J., Zhang, X., Tang, L., 2025. Three-dimensional MIL-88A(Fe)-derived α-Fe_2O_3 and graphene composite for efficient photo-Fenton-like degradation of ciprofloxacin. Chin Chem Lett, 111063. https://doi.org/10.1016/j.cclet.2025.111063.

[20] Mohammed, M.T.E., Djamel, N., Mohamed, T., Amokrane, S., 2021. Study of the adsorption of an organic pollutant onto a microporous metal organic framework. Water Sci Technol 83 (1), 137–151. https://doi.org/10.2166/wst.2020.566.

[21] Mukherjee, S., Sensharma, D., Qazvini, O.T., Dutta, S., Macreadie, L.K., Ghosh, S. K., Babarao, R., 2021. Advances in adsorptive separation of benzene and cyclohexane by metal-organic framework adsorbents. Coord Chem Rev 437, 213852. https://doi.org/10.1016/j.ccr.2021.213852.

[22] Sebak, M.A., Guizani, I., Gami, F., Mostafa, M., Mostafa, M.M., 2023. Photoluminescence and Fourier transform infrared spectral studies of varying levels of manganese doping in zinc phosphate oxide glasses. J Electron Mater 52 (7), 4551–4557. https://doi.org/10.1007/s11664-023-10389-8.

[23] Sun, K., Huang, Y., Sun, F., Wang, Q., Zhou, Y., Wang, J., Zhang, Q., Zheng, X., Fan, F., Luo, Y., Jiang, J., Jiang, H.-L., 2024. Dynamic structural twist in metal–organic frameworks enhances solar overall water splitting. Nat Chem 16 (10), 1638–1646. https://doi.org/10.1038/s41557-024-01599-6.

[24] Tsivion, E., Long, J.R., Head-Gordon, M., 2014. Hydrogen physisorption on Metal–Organic framework linkers and metalated linkers: a computational study of the factors that control binding strength. J Am Chem Soc 136 (51), 17827–17835. https://doi.org/10.1021/ja5101323.

[25] Valenzano, L., Civalleri, B., Chavan, S., Bordiga, S., Nilsen, M.H., Jakobsen, S., Lillerud, K.P., Lamberti, C., 2011. Disclosing the complex structure of UiO-66 metal organic framework: a synergic combination of experiment and theory. Chem Mater 23 (7), 1700–1718. https://doi.org/10.1021/cm1022882.

[26] Vellingiri, K., Kumar, P., Deep, A., Kim, K.-H., 2017. Metal-organic frameworks for the adsorption of gaseous toluene under ambient temperature and pressure. Chem Eng J 307, 1116–1126. https://doi.org/10.1016/j.cej.2016.09.012.

[27] Wang, R., Luan, X., Bao, J., Muhammad, Y., Jalil Shah, S., Wang, G., Li, J., Lin, G., Ji, H., Zhao, Z., 2023. Cr-N bridged MIL-101@tubular calcined N-doped polymer enhanced adsorption of vaporous toluene under high humidity. Sep Purif Technol 305, 122540. https://doi.org/10.1016/j.seppur.2022.122540.

[28] Wu, S., Chen, Z., Qian, Z., Zhang, Z., Sun, Y., Zhang, X., Tao, H., Zhang, Q., Xie, S., Wang, Y., Self-Healing Iridium-Doped Manganese Oxide for Boosting Stability of Acidic Oxygen Evolution. Advanced Functional Materials n/a(n/a), 2417766. https://doi.org/https://doi.org/10.1002/adfm.202417766.

[29] Xie, L.-H., Liu, X.-M., He, T., Li, J.-R., 2018. Metal-Organic frameworks for the capture of trace aromatic volatile organic compounds. Chem 4 (8), 1911–1927. https://doi.org/10.1016/j.chempr.2018.05.017.

[30] Xu, Y., Wang, P., Zhang, M., Dai, W., Xu, Y., Zou, J.-P., Luo, X., 2024. Constructing asymmetric dual active sites through symbiotic effect for achieving efficient and selective photoreduction of CO_2 to C_2H_4. Energy Environ Sci 17 (14), 5060–5069. https://doi.org/10.1039/D4EE01376J.

[31] Yang, H., Liu, G., Zheng, L., Zhang, M., Guan, Z., Liu, T., Yang, J., 2024. Cu-Fe bimetallic MOFs with long lifetime separated-state charge for enhancing selectivity for CO_2 photoreduction to CH_4. Appl Catal B Environ Energy 359, 124491. https://doi.org/10.1016/j.apcatb.2024.124491.

[32] Yang, L., He, X., Dincă, M., 2019. Triphenylene-Bridged trinuclear complexes of cu: models for spin interactions in Two-Dimensional electrically conductive Metal–Organic frameworks. J Am Chem Soc 141 (26), 10475–10480. https://doi.org/10.1021/jacs.9b04822.

[33] Yang, S., Wang, X., Song, G., Lu, G., Shi, G., Wang, Y., Xie, X., Sun, J., 2025. Ti-O-Mo bond-bridged PMA@MIL-125-NH_2 photocatalyst for gas acetone photocatalytic degradation. Appl Catal B Environ Energy 367, 125112. https://doi.org/10.1016/j.apcatb.2025.125112.

[34] Yang, Y., Hu, X., Wang, G., Han, J., Zhang, Q., Liu, W., Xie, Z., Zhou, Z., 2024. Two better than one: enhanced Photo-Assisted Li-O_2 batteries with bimetallic Fe-UiO-66 Metal-Organic framework photocathodes. Adv Funct Mater 34 (24). https://doi.org/10.1002/adfm.202315354.

[35] Yu, J., Wang, X., Chen, L., Lu, G., Shi, G., Xie, X., Wang, Y., Sun, J., 2022. Enhanced adsorption and visible-light photocatalytic degradation of toluene by CQDs/UiO-66 MOG with hierarchical pores. Chem Eng J 435, 135033. https://doi.org/10.1016/j.cej.2022.135033.

[36] Zhang, X., Gao, B., Creamer, A.E., Cao, C., Li, Y., 2017. Adsorption of VOCs onto engineered carbon materials: a review. J Hazard Mater 338, 102–123. https://doi.org/10.1016/j.jhazmat.2017.05.013.

[37] Zhang, X., Yang, Y., Song, L., Chen, J., Yang, Y., Wang, Y., 2019. Enhanced adsorption performance of gaseous toluene on defective UiO-66 metal organic framework: equilibrium and kinetic studies. J Hazard Mater 365, 597–605. https://doi.org/10.1016/j.jhazmat.2018.11.049.

[38] Zhou, G., Lei, B., Dong, F., 2024. Lewis acid sites in (110) Facet-Exposed BiOBr promote C–H activation and selective photocatalytic toluene oxidation. ACS Catal 14 (7), 4791–4798. https://doi.org/10.1021/acscatal.4c00877.

[39] Zhu, Y., Guo, F., Wei, Q., Lai, F., Chen, R., Guo, J., Gong, M., Zhang, S., Wang, Z., Zhong, J., He, G., Cheng, N., Engineering the Metal/Oxide Interfacial O-Filling Effect to Tailor Oxygen Spillover for Efficient Acidic Water Oxidation. Advanced Functional Materials n/a(n/a), 2421354. https://doi.org/https://doi.org/10.1002/adfm.202421354.